Volume 14
Number 10
14 March 2023
Pages 2471–2764

Chemical Science

rsc.li/chemical-science

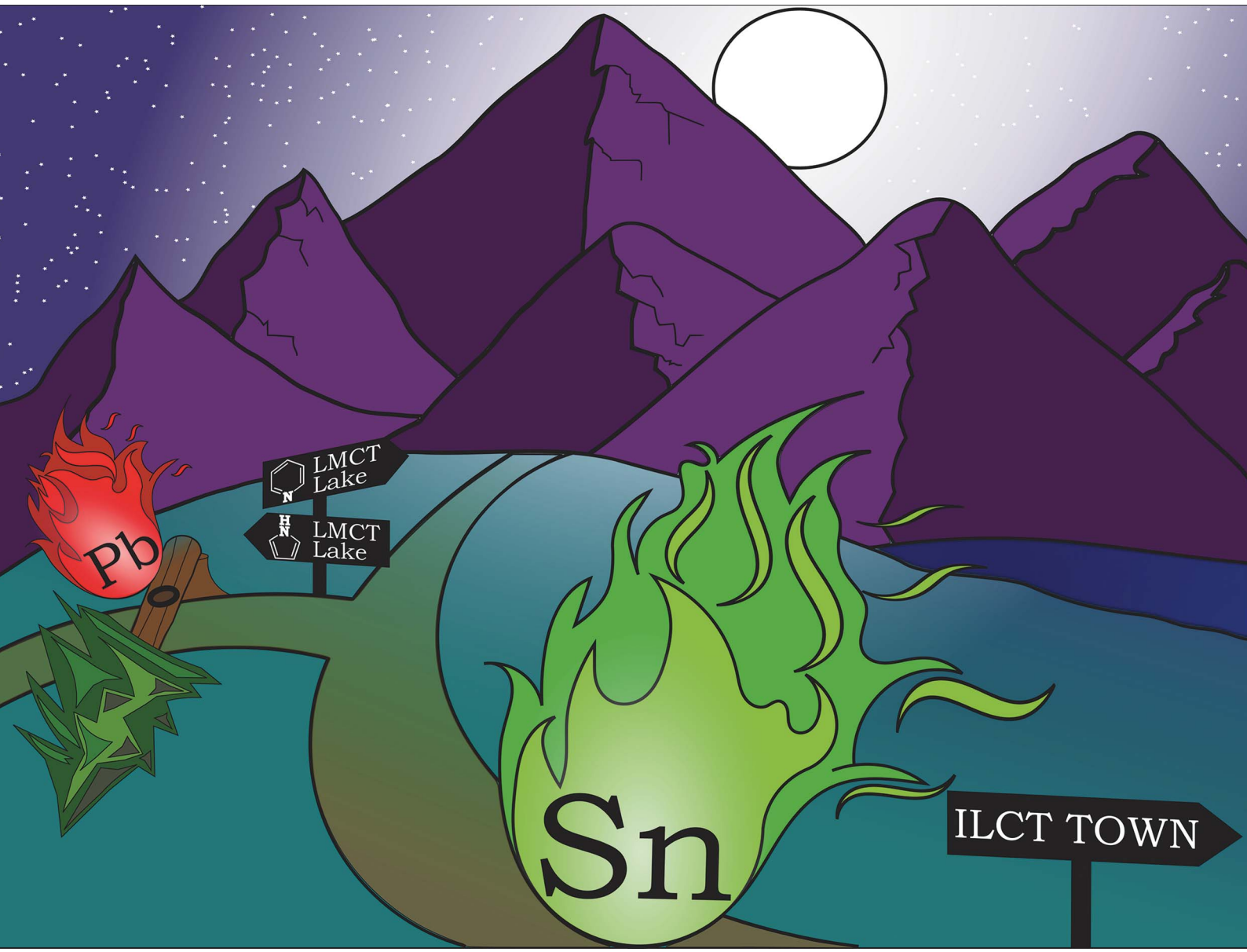

ISSN 2041-6539

ROYAL SOCIETY OF CHEMISTRY

EDGE ARTICLE

Christoph Förster, Katja Heinze *et al.*

Excited state energy landscape of phosphorescent group 14 complexes

Chemical Science

ROYAL SOCIETY OF CHEMISTRY

EDGE ARTICLE

View Article Online
View Journal | View Issue

Cite this: *Chem. Sci.*, 2023, **14**, 2489

All publication charges for this article have been paid for by the Royal Society of Chemistry

Received 20th December 2022
Accepted 27th January 2023

DOI: 10.1039/d2sc06984a

rsc.li/chemical-science

Excited state energy landscape of phosphorescent group 14 complexes†

Philipp Sikora, Robert Naumann, Christoph Förster * and Katja Heinze *

Great progress has been achieved on phosphorescent or photoactive complexes of the Earth-abundant transition metals, while examples for phosphorescent heavy main group element complexes are rare, in particular for group 14 complexes in the oxidation state +II. The known compounds often show only weak phosphorescence with fast non-radiative deactivation. The underlying photophysical processes and the nature of the phosphorescent electronic states have remained essentially unexplored. The present combined photophysical and theoretical study on tin(II) and lead(II) complexes E(bpep) with the dianionic tridentate ligand $bpep^{2-}$ (E = Sn, Pb; H_2bpep = 2-[1,1-bis(1*H*-pyrrol-2-yl)ethyl]pyridine) provides unprecedented insight in the excited state energy landscape of tetrel(II) complexes. The tin complex shows green intraligand charge transfer (ILCT) phosphorescence both in solution and in the solid state. In spite of its larger heavy-atom effect, the lead complex only shows very weak red phosphorescence from a strongly distorted ligand-to-metal charge transfer (LMCT) state at low temperatures in the solid state. Detailed (TD-)DFT calculations explain these observations and delineate the major path of non-radiative deactivation *via* distorted LMCT states. These novel insights provide rational design principles for tetrel(II) complexes with long-lived phosphorescence.

1 Introduction

Photoluminescent, in particular phosphorescent and photoactive transition metal complexes (TMCs) of the Earth-abundant elements, mainly 3d elements, evolved to a potential alternative to the precious elements, *e.g.* ruthenium, iridium or platinum.[1–5] The key prerequisite for applications in bimolecular photochemical reactions is a sufficiently long lifetime of the photoactive excited state (ES). This can be achieved for ESs with different spin multiplicities to the ground state (GS), rendering non-radiative and radiative processes between ES and GS spin-forbidden, thus extending the ES lifetime.[6] In order to access ESs of different spin multiplicity to the GS and the initially populated Franck–Condon state, intersystem crossing (ISC) must be effective. ISC rates increase for ES's wavefunctions with high metal character invoking spin–orbit coupling (SOC) by a heavy-atom effect or by effective spin–vibronic coupling.[7] The research on photoactive 3d or 4d TMCs envisaged mainly weakly distorted metal-to-ligand (MLCT) or ligand-to-metal charge transfer (LMCT) and intraconfigurational spin-flip states as potential photoactive states to invoke a high metal character for fast ISC.[1–3] In pseudo-octahedral $3d^n$ TMCs (n = 1–9) the high density of low-lying strongly distorted metal-centered (MC) states typically enables fast non-radiative deactivation of CT states.[1–3] For photoactive pseudo-tetrahedral d^{10} copper(I) complexes, the flattening distortion of the photoluminescent ^{3}MLCT states, can facilitate fast non-radiative deactivation.[8–10] The photoluminescence lifetimes of pseudo-tetrahedral copper(I) complexes are also very sensitive to coordinating solvents and anions in the flattened ^{3}MLCT states.[9,11] This illustrates the interplay between ES ordering and ES distortion, which depends on the coordination geometry and rigidification of the complex. For 3d TMCs, the underlying photophysical processes are well understood and groundbreaking progress was achieved in the last few years.[1–5]

Examples of heavy main group complexes, mainly group 14 and 15, showing beside conventional fluorescence,[12,13] phosphorescence and/or thermally activated delayed fluorescence (TADF),[10,14–16] are rare.[17–19] Emission is often limited to frozen solutions or even to the solid state, precluding bimolecular reactivity.[13,17–19] Complexes of group 15 elements, in particular bismuth(III) with $6s^2$ electron configuration, can show phosphorescence.[20–28] The oxidation state +IV dominates in tetrel group 14 complexes with potentially photoactive triplet states[29–35] and fluorescent or photoluminescent states of yet unknown character.[36–44] Photoluminescent tetrel(II) complexes are very scarce. Scandola and co-workers reported for $Pb(QO)_2$ **I** (QOH = 8-hydroxyquinoline) a weak green fluorescence and an even weaker red phosphorescence from intraligand (IL) states in *N*,*N*-dimethylformamide (DMF, 298 K; λ_f = 550 nm, τ_f = 0.4 ns, $\Phi_f \approx 0.003$;

Johannes Gutenberg University Mainz, Duesbergweg 10-14, 55128 Mainz, Germany. E-mail: christoph.foerster@uni-mainz.de; katja.heinze@uni-mainz.de

† Electronic supplementary information (ESI) available: Experimental procedures, spectral details, (TD-)DFT results. CCDC 2211125 and 2211126. For ESI and crystallographic data in CIF or other electronic format see DOI: https://doi.org/10.1039/d2sc06984a

$\lambda_p \approx 650$ nm, $\tau_p \approx 3$ μs, $\Phi_p < 0.0001$) and glassy ethanol (77 K; $\lambda_f = 510$ nm, $\tau_f < 20$ ns; $\lambda_p \approx 610$ nm, $\tau_p = 180$ μs), respectively (Scheme 1a).[45] The triplet state of the Pb complex **I** is efficiently quenched by energy transfer (EnT) in a bimolecular reaction with $[Cr(CN)_6]^{3-}$ in DMF with a quenching rate constant of $k_q = 3.7 \times 10^8$ M^{-1} s^{-1}.[45] Studies by Vogler and co-workers on photoluminescent halido germanium(II), tin(II) and lead(II) complexes $[EX_3]^-$ **II^{E,X}** (E = Ge–Pb: X = Cl; E = Sn, Pb: X = Br) and $[PbX_4]^{2-}$ **III^{X}** (X = Cl, Br) revealed phosphorescence from MC states at 510–604 nm after excitation with UV light in fluid acetonitrile solution (Scheme 1b).[46,47] The population of the emissive triplet state with a s^1p^1 electron configuration, is accompanied with large structural reorganization from C_{3v} to D_{3h} symmetry for $[EX_3]^-$ ions.[46] This distortion enables efficient non-radiative deactivation of the triplet state. In the series $[EX_3]^-$ (E = Ge–Pb, X = Cl, Br), the Sn complexes exhibit short photoluminescence lifetimes below the detection limit and the lowest quantum yields ($\Phi_p = 0.068$ (Cl); $\Phi_p = 0.0046$ (Br)) compared to Ge ($\Phi_p = 0.081$ (Cl)) and Pb ($\tau_p = 17$ μs, $\Phi_p = 0.159$ (Cl); $\Phi_p = 0.086$ (Br)).[46,47] Despite the short photoluminescence lifetime, $[SnCl_3]^-$ undergoes bimolecular photooxidation reactions to $SnOCl_2$ with oxygen after excitation with UV-C light ($\lambda_{ex} = 254$ nm).[48]

Bis(β-diketonato) lead(II) complexes **IV$^{R,R'}$** prepared by Vogler and co-workers show blue to green intraligand (IL) phosphorescence in the solid state. The phosphorescence is diminished in ethanol solution at r.t. The respective hexafluoroacetylacetonato tin(II) complex is not photoluminescent (Scheme 1c).[27,49] The very weak phosphorescence of the β-diketonato lead(II) complexes is attributed to a large geometric reorganization leading to fast non-radiative relaxation.[49] Unfortunately, no photoluminescence lifetimes and quantum yields were reported for these compounds. A series of coordination polymers of lead(II) with polydentate tetrazolato ligands are phosphorescent from ^{3}IL, ^{3}MC and ^{3}MLCT states with admixed ^{3}XLCT (halide-to-ligand CT) character. The photoluminescence lifetimes amount up to $\tau_p = 1.55$ ms and a maximum quantum yield of $\Phi_p = 0.165$ in the solid state.[50] The molecular congener **V** with 6,6′-bis(1*H*-tetrazol-5-yl)-2,2′-bipyridine as proligand shows ^{3}MLCT phosphorescence with significantly lower photoluminescence quantum yield in the solid state ($\lambda_p = 593$ nm, $\tau_p = 347.5$ μs, $\Phi_p = 0.02$; Scheme 1d).[50] Substituting a chlorido ligand with a weakly coordinating triflato (OTf^-) ligand, increases the fluorescence quantum yield of a dipyrromethene tin(II) complex from 0.04 (**VI^{Cl}**) to 0.42 (**VI^{OTf}**) with a slight bathochromic shift of the fluorescence from $\lambda_f = 518$ nm to $\lambda_f = 524$ nm (Scheme 1e).[51] The significant increase in quantum yield is ascribed on the basis of an inspection of the GS molecular orbitals from density functional theory (DFT) calculations to a shift of a non-photoluminescent MLCT state to higher energies upon stabilising the occupied non-bonding tin-centered orbital after Cl^-/OTf^- exchange.[51]

Heavy tetrel(II) complexes are related to tetrylenes, the heavier carbene homologues.[52–56] The singlet ground state of heavier tetrylenes is described by a metal-centered occupied orbital with high s-character and a vacant or donor stabilised orbital with high p-character (Fig. 1).[52–56] Clearly, MC, IL, LMCT, MLCT and ligand-to-ligand charge transfer (LL′CT) states with their respective ES distortions must be considered in exploring the energy landscape of electronic states with the focus on photoluminescent and in particular phosphorescent properties (Fig. 1).

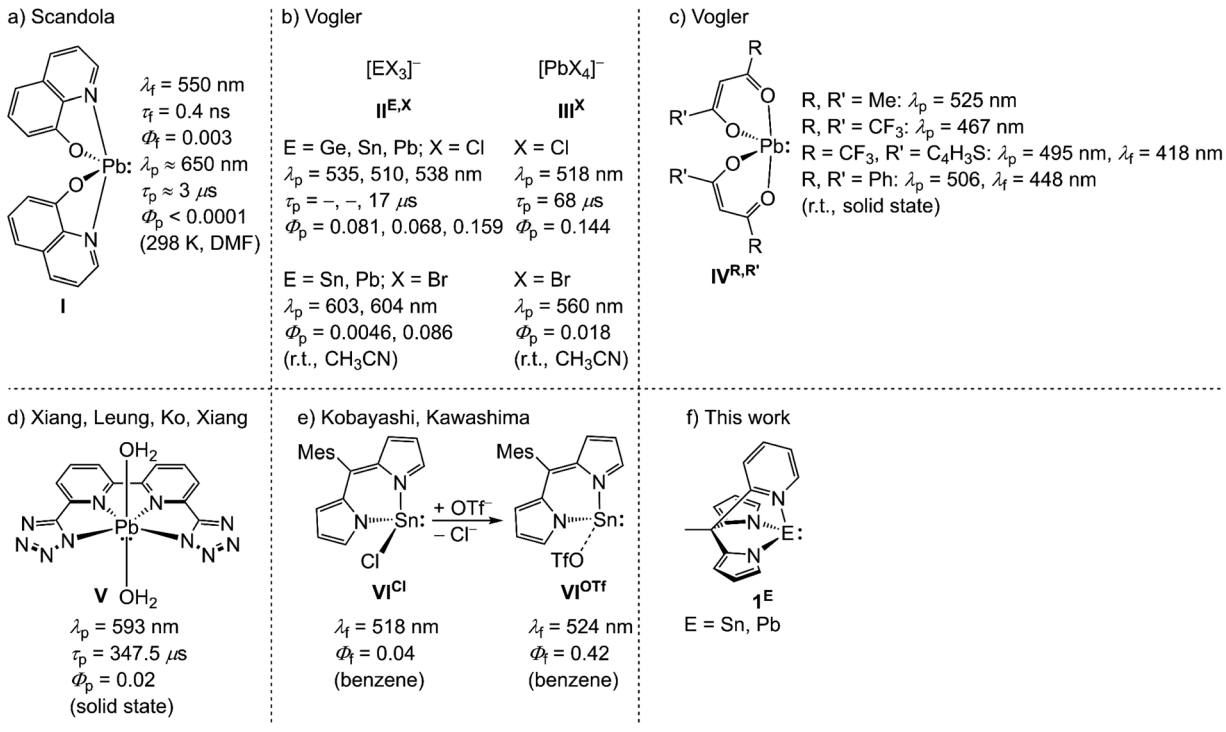

Scheme 1 Photoluminescent tetrel(II) complexes with selected photophysical data.

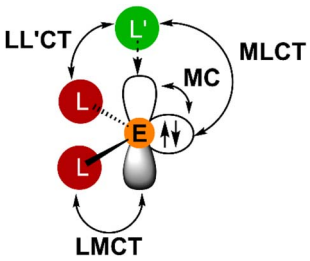

Fig. 1 Schematic representation of selected electronic transitions in donor (L′) stabilised homoleptic tetrylenes EL_2 (E = Si, Ge, Sn, Pb), excluding IL and other possible LMCT (L′ → E) and MLCT (E → L) transitions.

To the best of our knowledge, no combined experimental and quantum chemical studies are reported on the energy ordering and geometric distortions of excited states of photoluminescent tetrel(II) complexes. This study aims to shed more light on the underlying photophysical processes. The tripodal ligand bpep^{2-} (H_2bpep = 2-[1,1-bis(1*H*-pyrrol-2-yl)ethyl]pyridine)[57] with electron-rich pyrrolato and electron-poor pyridine donors in combination with the heaviest tetrels Sn and Pb for a large heavy-atom effect and fast ISC was chosen for this initial study (SOC constants: $\zeta(Sn) = 1855\ cm^{-1}$, $\zeta(Pb) = 5089\ cm^{-1}$).[58] Sn^{II}(bpep) **1^{Sn}** shows phosphorescence in the solid state and in solution, while the lead congener Pb^{II}(bpep) **1^{Pb}** with its larger heavy-atom effect is only very weakly photoluminescent. The elucidation of the different emission properties is supported by UV/vis absorption and variable-temperature steady-state and time-resolved emission spectroscopy as well as with detailed time-dependent (TD) DFT calculations.

2 Results and discussion

2.1. Synthesis, structural and spectroscopic properties

The tetrylenes E^{II}(bpep) (E = Sn **1^{Sn}**, Pb **1^{Pb}**) are synthesised *via* a transamination of H_2bpep[57] with bis[bis(trimethylsilyl)amido] tetrel(II) compounds $E^{II}[N(SiMe_3)_2]_2$ (ref. 59) in dichloromethane as colourless, moisture sensitive solids in 74% and 63% yields, respectively (Scheme 2). Complexes **1^{E}** are poorly soluble in most organic solvents. **1^{Sn}** is well soluble in tetrahydrofuran (THF) and sparsely in toluene, while **1^{Pb}** is only soluble in dimethylsulfoxide (DMSO) among the tested solvents. **1^{Sn}** and **1^{Pb}** are fully characterised by elemental analysis, ESI^+ mass spectrometry (ESI, Fig. S1 and S2†) and multinuclear (^{1}H, ^{13}C, ^{119}Sn, ^{207}Pb) NMR spectroscopy (ESI, Fig. S3–S14†). The ^{119}Sn resonance of **1^{Sn}** appears in the similar chemical shift range of other donor stabilised dipyrrolato stannylenes (ESI, Fig. S5†).[60] The solids of **1^{E}** are free of coordinating solvents, which could coordinate to the Sn or Pb atoms, as determined by ^{1}H NMR spectroscopy and elemental analyses. This speciation is important for the discussion of the photoluminescent properties in solution and in the solid state (ESI, Fig. S3 and S9†).

Crystals of **1^{Sn}**, suitable for X-ray diffraction analyses were obtained from hot toluene. **1^{Sn}** crystallises in the trigonal space group R_3 with two independent molecules **1^{Sn,A}** and **1^{Sn,B}** in the asymmetric unit (Fig. 2a; ESI, Fig. S15 and Table S1†). **1^{Sn,B}** is disordered with a pyrrolato/pyridine site occupation, so that the more precise structural parameters of **1^{Sn,A}** are discussed. Both molecules feature a distorted trigonal pyramidal coordination of the Sn atom. A further solid state structure of **1^{Sn}** could be determined from crystals, obtained from slow diethylether diffusion to a solution of **1^{Sn}** in a 1 : 1 mixture of 1,4-dioxane : tetrahydrofuran. Here, **1^{Sn}** forms a centrosymmetric 1,4-dioxane (diox) bridged dimer **(1^{Sn})$_2$(diox)** (monoclinic space group *I*2/*a*) leading to a four-coordinate tin(II) ion (Fig. 2b; ESI, Table S1†). This solid state structure indicates that **1^{Sn}** will likely form solvates in THF and THF/1,4-dioxane solutions. The 1,4-dioxane coordination with a Sn–O distance of 2.547(2) Å elongates the tin–nitrogen(pyridine) (Sn–N^{py}) bond from 2.317(5) Å (**1^{Sn}**) to 2.375(2) Å (**(1^{Sn})$_2$(diox)**). This Sn–N^{py} bond weakening arises from the competing interactions of the pyridine and 1,4-dioxane donors with the tetrel p-type orbital (Fig. 1; ESI Table S1†). This will also influence the photophysical properties of **1^{Sn}** (*vide infra*). The much lower solubility of **1^{Pb}** in most organic solvents prohibited growing single crystals suitable for X-ray diffraction analysis, but the NMR spectroscopic, mass spectrometric and analytical data confirm the composition and purity.

The structures of **1^{Sn}**, **1^{Sn}(thf)** and **1^{Pb}** were optimised by DFT (CPCM-(THF)-RIJCOSX-B3LYP-D3BJ-ZORA/def2-TZVPP/old-

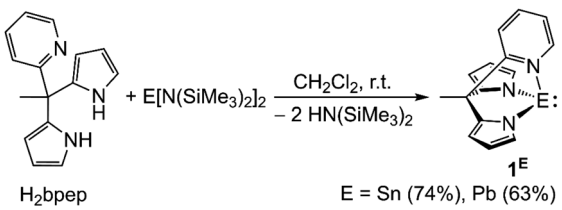

Scheme 2 Syntheses of stannylene and plumbylene E^{II}(bpep) (E = Sn **1^{Sn}**, Pb **1^{Pb}**) *via* transamination from $E[N(SiMe_3)_2]_2$ and H_2bpep, yields given in parentheses.

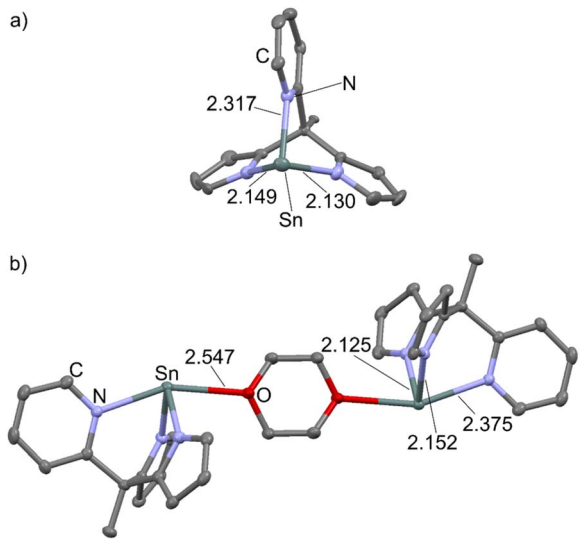

Fig. 2 Molecular structures of (a) **1^{Sn}** and (b) of the 1,4-dioxane bridged dimer **(1^{Sn})$_2$(diox)** with selected structural parameters in Å. H atoms omitted, thermal ellipsoids at 50% probability level.

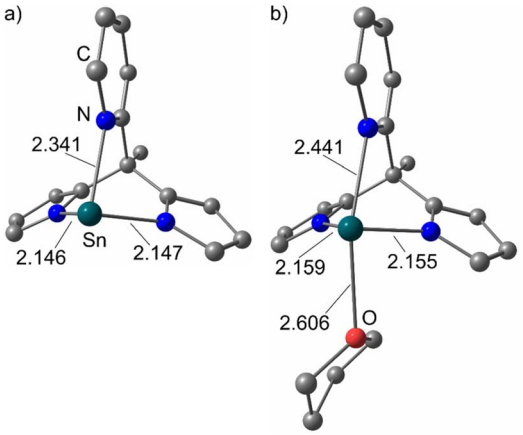

Fig. 3 DFT optimised structures of (a) $\mathbf{1}^{Sn}$ and (b) $\mathbf{1}^{Sn}$**(thf)** in the singlet ground state with selected structural parameters in Å (CPCM-(THF)-RIJCOSX-B3LYP-D3BJ-ZORA/def2-TZVPP/old-ZORA-TZVPP(Sn)).

ZORA-TZVPP(Sn)/SARC-ZORA-TZVPP(Pb)). The structural parameters are well reproduced by the DFT geometry optimised structures of $\mathbf{1}^{Sn}$ (Sn–N^{py}: 2.341 Å) and $\mathbf{1}^{Sn}$**(thf)** (Sn–O^{thf}: 2.606 Å, Sn–N^{py}: 2.441 Å) as a model for $(\mathbf{1}^{Sn})_2$**(diox)** (Fig. 3; ESI, Table S1†). To probe the presence of different tetrahydrofuran adducts, DFT calculations on $\mathbf{1}^{Sn}$**(thf)**$_2$ were additionally performed. Two isomers *cis*-$\mathbf{1}^{Sn}$**(thf)**$_2$ and *trans*-$\mathbf{1}^{Sn}$**(thf)**$_2$ could be localised as local minima on the potential energy surface as vander-Waals adducts between two and one THF molecules and $\mathbf{1}^{Sn}$ (ESI, Fig. S16†). The THF dissociation is exergonic with Gibbs free energies at 298 K for *cis*-/*trans*-$\mathbf{1}^{Sn}$**(thf)**$_2$ (*cis*: $\Delta G_{298} = -38$ kJ mol^{-1}, *trans*: $\Delta G_{298} = -47$ kJ mol^{-1}) to $\mathbf{1}^{Sn}$**(thf)** and THF and slightly exergonic for dissociation of $\mathbf{1}^{Sn}$**(thf)** ($\Delta G_{298} = -11$ kJ mol^{-1}). This indicates that the solvent-free complex $\mathbf{1}^{Sn}$ is the dominant species in solution. An exergonic Gibbs free dissociation energy of $\Delta G_{298} = -31$ kJ mol^{-1} was experimentally determined for the THF dissociation of a cyclic dialkylstannylene THF adduct, supporting the present DFT results.[61]

The UV/vis absorption spectra of $\mathbf{1}^{Sn}$ and $\mathbf{1}^{Pb}$ in THF and dimethylsulfoxide (DMSO), respectively, show several intense, broad, overlapping absorptions in the UV region tailing into the visible region with extinction coefficients $\varepsilon > 500$ M^{-1} cm^{-1} with $\lambda < 350$ nm (Fig. 4). TD-DFT calculations reveal several spin-allowed low-energy ^{1}ILCT transitions (412–303 nm) with significant oscillator strength between the electron-rich pyrrolato and electron-poor pyridine moieties for $\mathbf{1}^{Sn}$ (Fig. 4a; ESI, Fig. S17†). In addition, pyrrolato → Sn ^{1}LMCT (342, 288, 275 and 272 nm) transitions at similar energies are observed, which might play a role in the dynamics of $\mathbf{1}^{Sn}$ (*vide infra*). Sn → pyridine ^{1}MLCT (271 and 234 nm) and mixed ^{1}(ILCT/LMCT) (319 and 316 nm) transitions, as well as ^{1}MC (225 nm) transitions are found at higher energies at the Franck–Condon geometry. The TD-DFT spectrum of $\mathbf{1}^{Pb}$ features ^{1}ILCT transitions (409–305 nm) at very similar energies as found for $\mathbf{1}^{Sn}$, indicating that the central ion does not significantly affect these ligand-centered ^{1}CT transitions. ^{1}LMCT and mixed ^{1}(ILCT/LMCT) transitions of $\mathbf{1}^{Pb}$ are found at lower energies with 367 and 342 nm, respectively, closer to the lowest ^{1}ILCT transitions (Fig. 4b; ESI, Fig. S18,† ^{1}MLCT

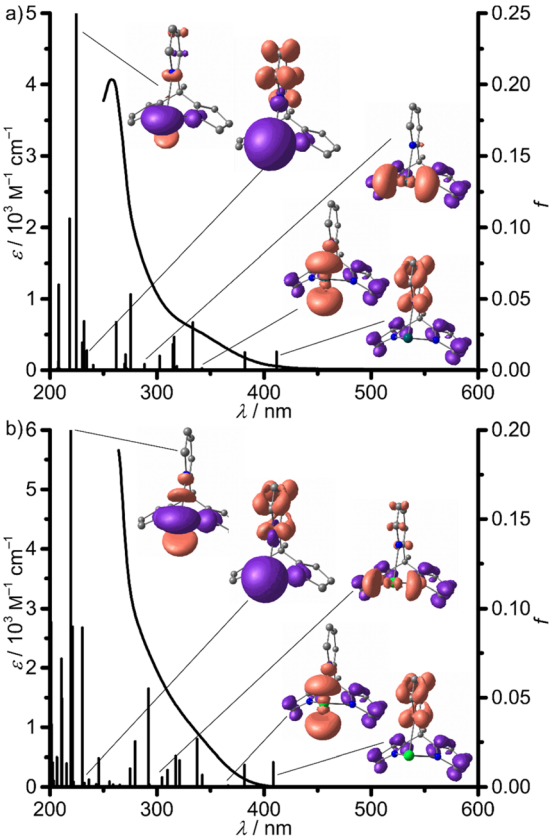

Fig. 4 UV/vis absorption spectra at 293 K of (a) $\mathbf{1}^{Sn}$ in tetrahydrofuran and of (b) $\mathbf{1}^{Pb}$ in dimethylsulfoxide with TD-DFT calculated oscillator strengths on $\mathbf{1}^{E}$ and difference electron densities of selected characteristic spin-allowed transitions (isosurface value 0.005 a.u., purple = electron loss, orange = electron gain, CPCM-(THF)-RIJCOSX-B3LYP-D3BJ-ZORA/def2-TZVPP/old-ZORA-TZVPP(Sn)/SARC-ZORA-TZVPP(Pb)).

(237 nm), ^{1}MC (220 nm)). The lower ^{1}LMCT transition energies of $\mathbf{1}^{Pb}$ are attributed to weaker Pb–N^{py} and lead–nitrogen(pyrrolato) bonds Pb–N^{pyr}, associated with a lowering of the vacant σ*-orbitals (LUMO+1, LUMO+3) with high p(Pb)-character with respect to the derivative $\mathbf{1}^{Sn}$ (LUMO+2, LUMO+3, Fig. 1; ESI, Fig. S19, S20 and Tables S1, S2†).

The investigation of the emission properties revealed a very weak photoluminescence of $\mathbf{1}^{Sn}$ at $\lambda_{em,293} = 611$ nm after excitation at $\lambda_{exc} = 325$ nm in 2-methyl-tetrahydrofuran (2-Me-THF) solution at 293 K (Fig. 5 and Table 1). Unfortunately, unidentified impurities in different batches of commercial spectroscopic grade 2-Me-THF and THF show photoluminescence in the UV with $\lambda_{em} < 400$ nm tailing into the weak emission of $\mathbf{1}^{Sn}$ after excitation at the same wavelength (Fig. 5b; ESI, Fig. S21†). Variable-temperature emission spectra of $\mathbf{1}^{Sn}$ in 2-Me-THF in a temperature range of 293–77 K show a significant increase in emission intensity and a blue-shift of the emission maximum from $\lambda_{em,293} = 611$ nm in fluid solution at 293 K to $\lambda_{em,77} = 523$ nm in frozen solution at 77 K (Fig. 5 and Table 1). This is probably a consequence of a rigidochromic effect.[62] The excitation spectra at 293 and 77 K largely follow the absorption spectrum at the low energy part (Fig. 4; ESI, Fig. S22†). Due to the

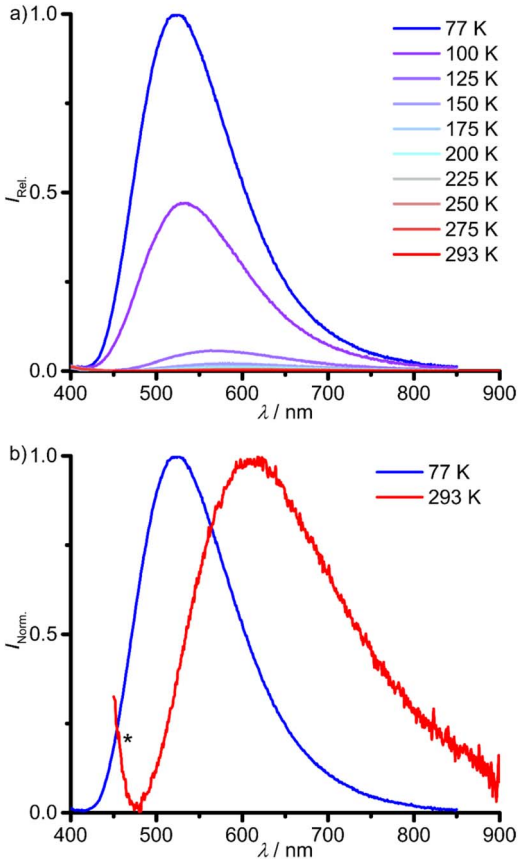

Fig. 5 (a) Temperature-dependent photoluminescence spectra of $\mathbf{1}^{Sn}$ in deaerated 2-Me-THF between 77 K (blue) and 293 K (red) with λ_{exc} = 325 nm and (b) the normalised emission spectra at 77 K and 293 K. The asterisk denotes the emission of an unidentified impurity in 2-Me-THF.

Table 1 Emission properties of $\mathbf{1}^{Sn}$ and $\mathbf{1}^{Pb}$

	λ_p/nm	τ_p	Φ_p
$\mathbf{1}^{Sn}$			
293 K[a]	611	≤ 8 ns (n.d.[c])	n.d.[c]
77 K[a]	523	2.0 (37%), 0.5 (43%), 0.1 (20%) ms[d]	n.d.[c]
293 K[b]	535	14 ns	0.005
77 K[b]	504	3.6 ms	0.58
$\mathbf{1}^{Pb}$			
77 K[b]	700	92 ns	0.0024

[a] 2-Me-THF solution. [b] Solid state. [c] Not detectable. [d] Relative emission amplitudes in parentheses.

weak photoluminescence, high concentrations had to be used, which cause spectral distortion in the high energy range. The photoluminescence lifetime measurements of $\mathbf{1}^{Sn}$ in fluid solution in the 125–293 K range gives ambiguous results due to the contribution of the photoluminescent impurity in 2-Me-THF. The determined lifetimes in the nanosecond range coincide with the emission of the unidentified impurity in 2-Me-THF (τ_{em} = 8 ns at 125 K). Hence, the photoluminescence lifetime of $\mathbf{1}^{Sn}$ might be in a similar or smaller order of magnitude as rough estimate (ESI, Fig. S23†). The fluorescent impurity in 2-Me-THF, the very weak emission of $\mathbf{1}^{Sn}$ at room temperature and the low solubility of $\mathbf{1}^{Sn}$ in other solvents prevented the photoluminescence quantum yield determination in solution.

The photoluminescence lifetime of $\mathbf{1}^{Sn}$ drastically increases to the millisecond range in frozen solution. The emission decay trace at 77 K is described with three lifetimes in the millisecond range (τ_1 = 2.0 ms, τ_2 = 0.5 ms, τ_3 = 0.1 ms; Table 1). At 100 K, the lifetimes drop by one order of magnitude with τ_3 vanishing in the instrument response function (IRF, τ_1 = 0.1 ms, τ_2 = 0.03 ms; Table 1; ESI, Fig. S24†). The strong temperature dependence of the photoluminescence lifetimes is associated to thermally activated non-radiative deactivation processes, which become dominant at elevated temperatures, even in frozen solution. Competing photophysical processes of different $\mathbf{1}^{Sn}$**(2-Me-thf)**$_n$ adducts with varying number of coordinated 2-Me-THF molecules in (frozen) solution might account for a bi- or triexponential photoluminescence decay. The very long photoluminescence lifetime at 77 K assigns the emission to a phosphorescence process, *i.e.* emission from a triplet state. According to DFT calculations, phosphorescence occurs from a rather nested ^{3}ILCT state (*vide infra*).

Solid donor solvent-free $\mathbf{1}^{Sn}$ emits at shorter wavelength $\lambda_{p,293}$ = 535 nm (293 K) and with a similar band shape as in solution (Fig. 5, 6a and Table 1). The emission blue-shifts to $\lambda_{p,77}$ = 504 nm upon cooling to 77 K (Fig. 6a and Table 1). The phosphorescence lifetimes from monoexponential fits and the photoluminescence quantum yields are determined to $\tau_{p,293}$ = 14 ns, $\Phi_{p,293}$ = 0.005 and $\tau_{p,77}$ = 3.6 ms, $\Phi_{p,77}$ = 0.58 at 293 and 77 K, respectively (Table 1; ESI, Fig. S25†).

The strong temperature dependence of the photoluminescence lifetime and yield is attributed to thermally activated non-radiative processes. According to the high phosphorescence quantum yield at 77 K, ^{1}ES → ^{3}ES ISC should be very efficient. Hence, non-radiative ES deactivation occurs mainly from the triplet ES. An Arrhenius plot of the photoluminescence rate constants ($k(T) = 1/\tau_p(T)$) is fitted as a sum of three rate constants $k_0/k_1/k_2$ (eqn (1) and Fig. 6b).[63] k_0 includes non-thermally activated radiative and non-radiative processes, while $k_1(T)$ and $k_2(T)$ are temperature dependent, expressed as Arrhenius equations with frequency factors A_1/A_2 and activation energies E_{a_1}/E_{a_2} (eqn (1)).

$$\frac{1}{\tau_p(T)} = k(T) = k_0 + k_1(T) + k_2(T) = k_0 + A_1 e^{-\frac{E_{a_1}}{RT}} + A_2 e^{-\frac{E_{a_2}}{RT}} \quad (1)$$

The obtained fit parameters indicate two thermally activated processes depopulating the photoluminescent state with barriers of E_{a_1} = 0.25 eV (2000 cm^{-1}), dominating the high temperature regime and E_{a_2} = 0.10 eV (810 cm^{-1}), dominant in the low temperature regime (Fig. 6b and Table 2).

Thermally activated depopulation of the photoluminescent state *via* two non-emissive ESs at similar activation energies has been observed for Rh^{III} complexes.[63]

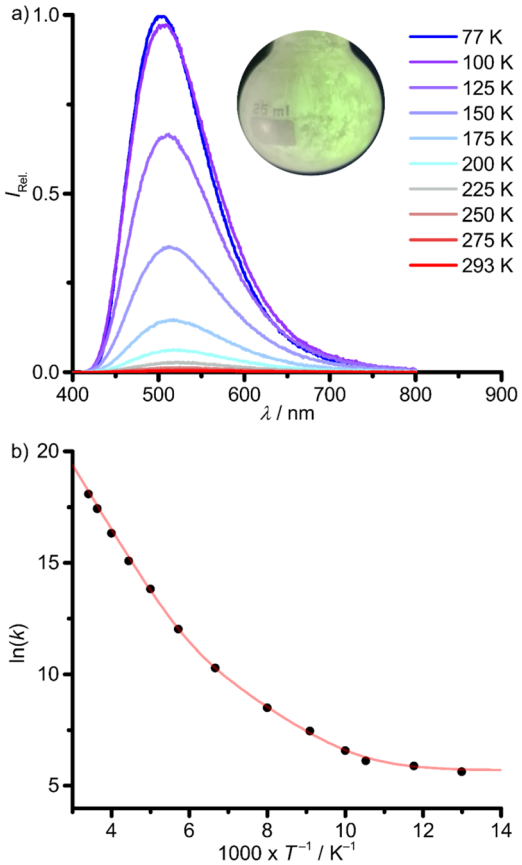

Fig. 6 (a) Temperature-dependent photoluminescence spectra of $\mathbf{1}^{Sn}$ in the solid state between 77 K (blue) and 293 K (red) with λ_{exc} = 350 nm (inset: photograph of the green photoluminescence at *ca.* 77 K) and (b) Arrhenius plot of the photoluminescence rate constants ($k(T) = 1/\tau_p(T)$, T = 77–293 K) with fit (red curve), according to eqn (1).

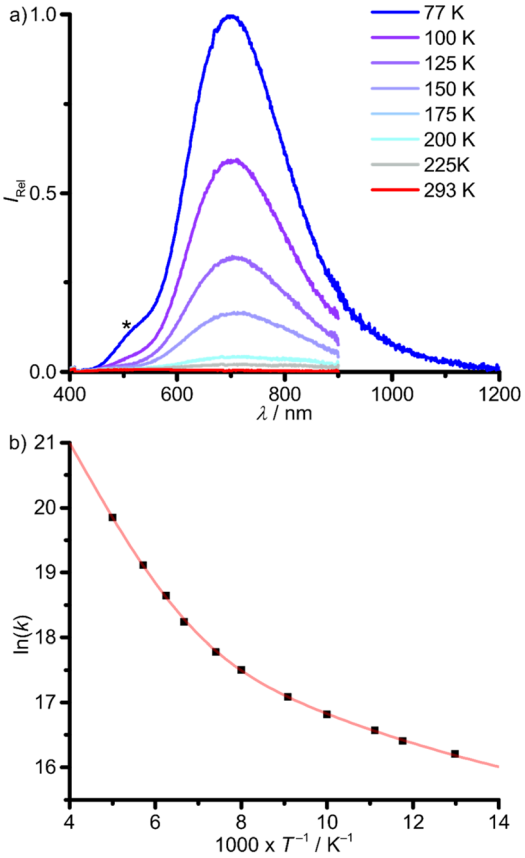

Fig. 7 (a) Temperature-dependent photoluminescence spectra of $\mathbf{1}^{Pb}$ in the solid state between 77 K (blue) and 200 K (red) with λ_{exc} = 350 nm. The spectrum at 77 K is composed of two spectra, measured with different detectors. The asterisk denotes the photoluminescence of an unidentified minor impurity (oxidation or solvolysis product of $\mathbf{1}^{Pb}$). (b) Arrhenius plot of the photoluminescence rate constants ($k(T) = 1/\tau_p(T)$, T = 77–200 K) with fit (red curve), according to eqn (1).

Table 2 Fit parameters for the emission decays of solid $\mathbf{1}^{Sn}$ and $\mathbf{1}^{Pb}$, obtained from Arrhenius plots, according to eqn (1)

	$\mathbf{1}^{Sn}$	$\mathbf{1}^{Pb}$
k_0/s^{-1}	298	3.77×10^6
E_{a_1}/eV (cm^{-1})	0.25 (2000)	0.11 (890)
E_{a_2}/eV (cm^{-1})	0.10 (810)	0.02 (200)
A_1/s^{-1}	1.57×10^{12}	1.88×10^{11}
A_2/s^{-1}	6.14×10^7	2.62×10^8

In contrast, $\mathbf{1}^{Pb}$ shows no photoluminescence in fluid DMSO solution at r.t. The low solubility of $\mathbf{1}^{Pb}$ in glass forming solvents prevented the investigation of the photoluminescence properties in solution at low temperatures. Yet, $\mathbf{1}^{Pb}$ shows a weak phosphorescence with $\lambda_{p,77}$ = 700 nm in the solid state at 77 K. Raising the temperature shifts the emission to lower energies with a strong loss of intensity ($\lambda_{p,200}$ = 720 nm, Fig. 7a). A minor impurity, below the NMR detection limit, with λ_{em} = 500 nm is ascribed to hydrolysis or oxidation products of $\mathbf{1}^{Pb}$, indicated by an asterisk in Fig. 7a. This assignment was verified by measuring the sample again after contact to air, showing a decrease of the band at ≈700 nm and an increase of the band at ≈500 nm (ESI, Fig. S26†).

The photoluminescence lifetimes of $\mathbf{1}^{Pb}$ determined from monoexponential fits drop from $\tau_{p,77}$ = 92 ns to $\tau_{p,200}$ = 2.4 ns upon warming from 77 to 200 K, respectively, with a very small photoluminescence quantum yield of $\Phi_{p,77}$ = 0.0024 at 77 K (ESI, Fig. S27†). Two activation barriers E_{a_1} = 0.11 eV (890 cm^{-1}) and E_{a_2} = 0.02 eV (200 cm^{-1}) could be extracted from an Arrhenius plot of the photoluminescence rate constants ($k(T) = 1/\tau_p(T)$, eqn (1), Fig. 7b and Table 2). The much larger rate constant k_0 of $\mathbf{1}^{Pb}$ (3.77×10^6 s^{-1}) *vs.* $\mathbf{1}^{Sn}$ (298 s^{-1}) includes non-thermally activated radiative and non-radiative processes and will be discussed in the context of DFT calculations (*vide infra*). The phosphorescence of $\mathbf{1}^{Pb}$ in the solid state at 77 K ($\lambda_{p,77}$ = 700 nm, 14 300 cm^{-1}) occurs at significantly lower energy as that of $\mathbf{1}^{Sn}$ ($\lambda_{p,77}$ = 504 nm, 19 800 cm^{-1}), despite the very similar absorption spectra (Fig. 4, 6a and 7a). Hence, the emissive states must be of different nature. DFT calculations serve to assign the different emissive states (*vide infra*).

2.2. Quantum chemical investigations

From the TD-DFT analysis, it becomes clear that excitation with 325 and 350 nm as used in the experimental setups populates a number of singlet states with different character in the Franck–Condon region, including ^{1}ILCT and ^{1}LMCT states (Fig. 4). It is likely that ISC is very fast and efficient due to the primary heavy atom effect *via* very large SOC of Sn and Pb (SOC constants: ζ(Sn) = 1855 cm^{-1}, ζ(Pb) = 5089 cm^{-1}).[58] Consequently, we focus in the following discussion on the triplet states of $\mathbf{1}^{\mathbf{Sn}}$ and $\mathbf{1}^{\mathbf{Pb}}$ only. In order to shed light onto the divergent emission properties of the tin and lead complexes, DFT calculations were performed on the triplet states (CPCM-(THF)-RIJCOSX-UB3LYP-D3BJ-ZORA/def2-TZVPP/old-ZORA-TZVPP(Sn)/SARC-ZORA-TZVPP(Pb)). In both cases, three triplet states with distinct structural features could be located, namely ^{3}ILCT, ^{3}LMCT$_{py}$ and ^{3}LMCT$_{pyr}$ states. The ^{3}ILCT state is essentially nested with the ^{1}GS. The major ^{1}GS to ^{3}ILCT state geometric reorganization is an E–N^{py} bond contraction with a slight E–N^{pyr} elongation with parallel decrease of the angle between the pyrrolate mean-square planes from 130° to 106° (ESI, Tables S1 and S2†). The ^{3}LMCT$_{py}$ and ^{3}LMCT$_{pyr}$ states (py = pyridine and pyr = pyrrolato) are strongly distorted with broken E–N^{py} and E–N^{pyr} bonds, respectively, in addition to a tilting of the respective heterocyclic pyridine or pyrrolate rings (Fig. 8–10). The ^{3}LMCT$_{py}$ state possesses the lowest energy in both complexes. The next higher state is ^{3}ILCT and ^{3}LMCT$_{pyr}$ for the tin and lead derivatives, respectively (Table 3).

^{3}ILCT → ^{3}LMCT$_{py}$ and ^{3}ILCT → ^{3}LMCT$_{pyr}$ DFT optimized transition states were located for $\mathbf{1}^{\mathbf{Sn}}$ giving activation barriers of 0.23 and 0.29 eV, respectively (Table 3 and Fig. 8). A much lower ^{3}ILCT → ^{3}LMCT$_{py}$ activation barrier of 0.06 eV was found for $\mathbf{1}^{\mathbf{Pb}}$, while no ^{3}ILCT → ^{3}LMCT$_{pyr}$ transition state could be located in this case (Fig. 9a). 2D maps of the triplet surfaces projected along the E–N^{py} and E–N^{pyr} modes were calculated on a lower level of theory for $\mathbf{1}^{\mathbf{Sn}}$ and $\mathbf{1}^{\mathbf{Pb}}$ (Fig. 10). The map of $\mathbf{1}^{\mathbf{Sn}}$

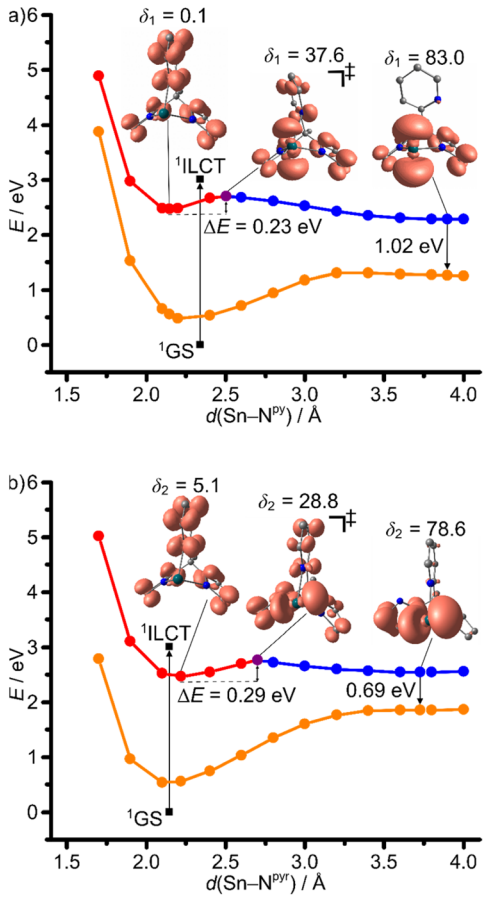

Fig. 8 Relaxed potential energy surface scans as projections along the (a) Sn–N^{py} and (b) Sn–N^{pyr} stretching modes on the triplet hypersurface $^3\mathbf{1}^{\mathbf{Sn}}$ with selected geometry optimised molecular structures with spin densities (isosurface value: 0.005 a.u.) and single point energies on singlet GS hypersurface $^1\mathbf{1}^{\mathbf{Sn}}$ at $^3\mathbf{1}^{\mathbf{Sn}}$ geometries (SCF energies). Selected Sn–N$^{py/pyr}$–C$^{py/pyr}$–C^{backbone} dihedral angles δ_1/δ_2 in deg. are indicated. ^{3}ILCT states in red, triplet transition states ^{3}ILCT → ^{3}LMCT$_{py}$ (a) and ^{3}ILCT → ^{3}LMCT$_{pyr}$ (b) in purple, ^{3}LMCT$_{py}$/^{3}LMCT$_{pyr}$ states in blue and ^{1}GS in orange. Vertical transition from relaxed ^{1}GS to the ^{1}ILCT state from TD-DFT calculations (3.01 eV) indicated as black arrow. CPCM-(THF)-RIJCOSX-(U)B3LYP-D3BJ-ZORA/def2-TZVPP/old-ZORA-TZVPP(Sn).

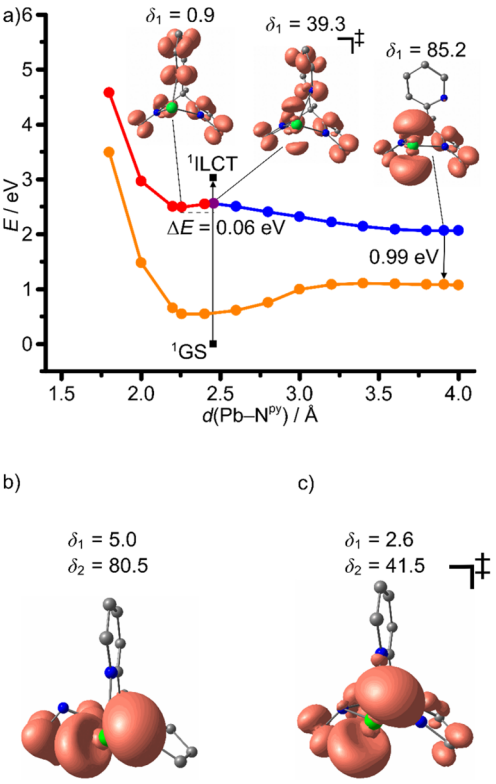

Fig. 9 (a) Relaxed potential energy surface scan as projection along the Pb–N^{py} stretching mode on the triplet hypersurface $^3\mathbf{1}^{\mathbf{Pb}}$ with selected geometry optimised molecular structures with spin densities (isosurface value: 0.005 a.u.) and single point energies on singlet GS hypersurface $^1\mathbf{1}^{\mathbf{Pb}}$ at $^3\mathbf{1}^{\mathbf{Pb}}$ geometries (SCF energies). Selected Pb–N^{py}–C^{py}–C^{backbone} dihedral angles δ_1 in deg. are indicated. ^{3}ILCT state in red, triplet transition state ^{3}ILCT → ^{3}LMCT$_{py}$ in purple, ^{3}LMCT$_{py}$ state in blue and ^{1}GS in orange. Vertical transition from relaxed ^{1}GS to the ^{1}ILCT state from TD-DFT calculations (3.03 eV) indicated as black arrow. Molecular structures with spin densities (isosurface value: 0.005 a.u.) and Pb–N$^{py/pyr}$–C$^{py/pyr}$–C^{backbone} dihedral angles δ_1/δ_2 in deg. of (b) the ^{3}LMCT$_{pyr}$ state and of (c) the ^{3}LMCT$_{py}$/^{3}LMCT$_{pyr}$ transition state, respectively. CPCM-(THF)-RIJCOSX-(U)B3LYP-D3BJ-ZORA/def2-TZVPP/SARC-ZORA-TZVPP(Pb).

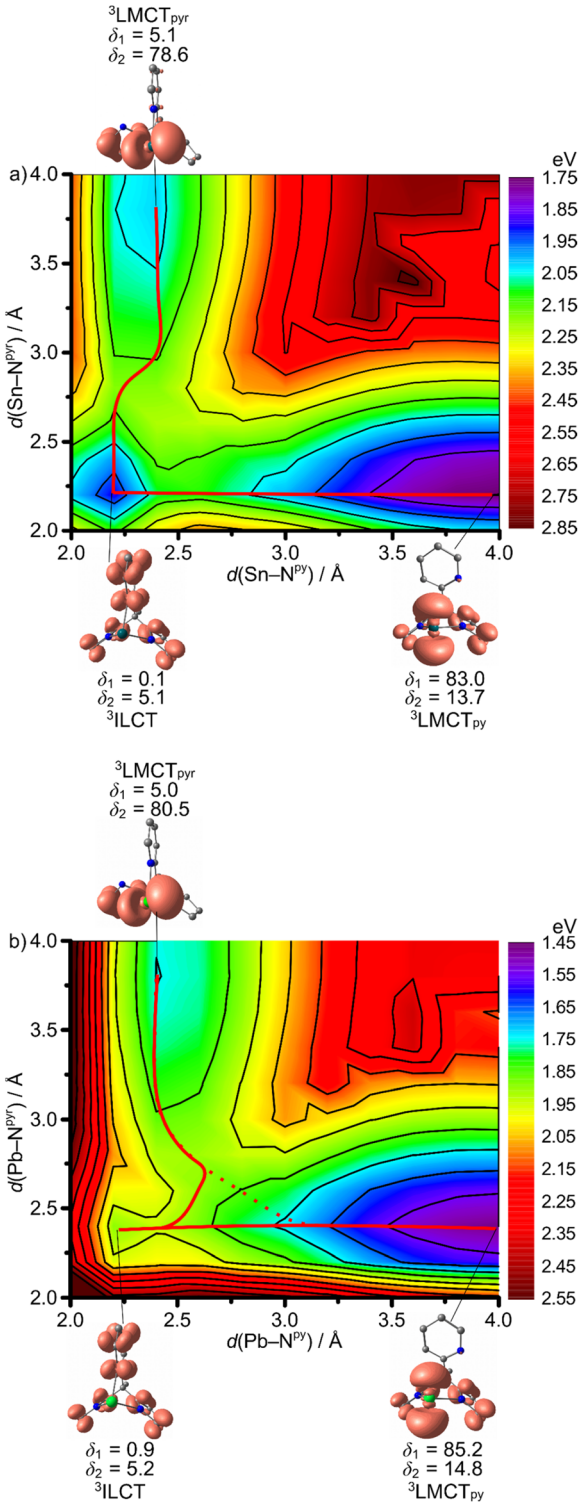

Fig. 10 Contour plots of 2D relaxed potential energy surface scans as projection along the E–N^{py} and E–N^{pyr} stretching modes on the triplet hypersurface $^3\mathbf{1}^E$ with selected geometry optimised molecular structures with spin densities (isosurface value: 0.005 a.u.) of (a) $\mathbf{1}^{Sn}$ and (b) $\mathbf{1}^{Pb}$. Selected E–N$^{py/pyr}$–C$^{py/pyr}$–C^{backbone} dihedral angles δ_1/δ_2 in deg. are indicated and the graphically determined, estimated minimum energy paths for ^{3}ILCT → ^{3}LMCT$_{py}$/^{3}LMCT$_{pyr}$ (red lines) and ^{3}LMCT$_{py}$/^{3}LMCT$_{pyr}$ internal conversion (dotted line). Energies are given *vs.* the ^{1}GS energy (ESI, Fig. S28†). CPCM-(THF)-RIJCOSX-UB3LYP-D3BJ-ZORA/def2-TZVPP/old-ZORA-TZVPP(Sn)/SARC-ZORA-TZVPP(Pb).

Table 3 Relative energies (SCF)[a] of triplet states, ^{1}GS and transition states (TS) in eV, calculated by DFT for $\mathbf{1}^{Sn}$ and $\mathbf{1}^{Pb}$

	$\mathbf{1}^{Sn}$	$\mathbf{1}^{Pb}$
^{3}ILCT	0	0
^{3}LMCT$_{py}$	−0.19	−0.43
^{3}LMCT$_{pyr}$	+0.08	−0.15
^{1}GS$_{relaxed}$[b]	−2.47	−2.49
^{1}GS$_{^3ILCT\text{-}geom}$[c]	−1.91	−1.94
^{1}GS$_{^3LMCT_{py}\text{-}geom}$[c]	−1.21	−1.42
^{1}GS$_{^3LMCT_{pyr}\text{-}geom}$[c]	−0.61	−0.95
TS(^{3}ILCT → ^{3}LMCT$_{py}$)	+0.23	+0.06
TS(^{3}ILCT → ^{3}LMCT$_{pyr}$)	+0.29	—
TS(^{3}LMCT$_{py}$ → ^{3}LMCT$_{pyr}$)[d]	—	+0.46

[a] For Gibbs free energies, see: ESI, Table S3. [b] Relaxed geometry. [c] ^{1}GS at relaxed ^{3}ILCT, ^{3}LMCT$_{py}$ and ^{3}LMCT$_{pyr}$ geometry, respectively. [d] Relative energy to the relaxed ^{3}LMCT$_{py}$ state.

clearly shows two trajectories from the ^{3}ILCT state to the ^{3}LMCT states along minimum energy paths (Fig. 10a). In contrast, the map of $\mathbf{1}^{Pb}$ discloses only a single minimum energy trajectory from the ^{3}ILCT state towards the ^{3}LMCT$_{py}$ state, but suggests a (higher energy) path from the ^{3}LMCT$_{py}$ to the ^{3}LMCT$_{pyr}$ state (Fig. 10b). This excited state landscape explains the failure to locate a ^{3}ILCT → ^{3}LMCT$_{pyr}$ transition state for $\mathbf{1}^{Pb}$.

Assuming that the dynamics after ISC on the triplet surface start at the respective relaxed ^{3}ILCT states, the different barriers to the ^{3}LMCT states of 0.23/0.29 eV and 0.06 eV for $\mathbf{1}^{Sn}$ and $\mathbf{1}^{Pb}$, respectively, will determine the following dynamics (Table 3). Without emphasising the calculated numbers too strongly, we note that for $\mathbf{1}^{Sn}$ an experimental barrier of E_{a_1} = 0.25 eV has been determined close the calculated values (Tables 2 and 3). As the ^{3}LMCT$_{pyr}$ state lies above the ^{3}ILCT state, we assign the observed temperature-dependent emission of $\mathbf{1}^{Sn}$ at 535 nm to the ^{3}ILCT state and the observed barrier to the ^{3}ILCT → ^{3}LMCT$_{py}$ population transfer. Consequently, the emission of $\mathbf{1}^{Sn}$ is a non-Kasha emission due to a significant barrier to the lower energy triplet state (^{3}LMCT$_{py}$).

On the other hand, the very small ^{3}ILCT → ^{3}LMCT$_{py}$ barrier calculated for $\mathbf{1}^{Pb}$ suggests that rapid evolution to the ^{3}LMCT$_{py}$ state occurs along with Pb–N^{py} bond elongation and dissociation. This strongly distorted state at low energy can rapidly decay back to the ^{1}GS, which fits to the experimental observations of a weak, short-lived, low-energy emission of $\mathbf{1}^{Pb}$ (Table 1). The ^{3}LMCT$_{pyr}$ state of $\mathbf{1}^{Pb}$ lies above the ^{3}LMCT$_{py}$ state and the ^{3}LMCT$_{py}$ → ^{3}LMCT$_{pyr}$ barrier of 0.46 eV impedes its significant population leading to the assignment of the observed low-energy emission as originating from the ^{3}LMCT$_{py}$ state (Table 3 and Fig. 9b, c). The other small barriers of 0.02–0.11 eV observed in the photoluminescence decays of $\mathbf{1}^{Sn}$ and $\mathbf{1}^{Pb}$ might be associated to other modes that promote the ISC from the triplet states to the ^{1}GS (Table 2). These enabling modes are not covered in our calculations (Table 3).

It is to note, in the frame of these DFT calculations the rigid environment of a solid with constrained geometric reorganisation is not fully described and the barriers and ES energies might be higher due to externally forced rigidification. Yet,

distinct geometric flexibility in the solid state has been discussed for photo-switches[64] and photoluminescent copper(I) complexes.[65] On the other hand, rigidification by aggregation significantly impacts the GS and ES potential energy surfaces, *e.g.* raising the energy of conical intersections and surface crossing points, which leads to aggregation-induced emission[66,67] and in particular, aggregation-induced phosphorescence.[18,68] The molecular flexibility in the solid state of $\mathbf{1}^{\mathbf{Sn}}$ and in particular of $\mathbf{1}^{\mathbf{Pb}}$ might be sufficient for thermally activated depopulation of the ^{3}ILCT state *via* the lower-lying ^{3}LMCT states. However, the lifetime and energy of the $^3LMCT_{py}$ state are sufficiently high to observe the very weak phosphorescence of $\mathbf{1}^{\mathbf{Pb}}$ at low temperatures (Fig. 7).

The experimental rate constant $k_0 = 298\ s^{-1}$ of $\mathbf{1}^{\mathbf{Sn}}$ is much smaller than $k_0 = 3.77 \times 10^6\ s^{-1}$ of $\mathbf{1}^{\mathbf{Pb}}$. This finding might be associated with the different vertical energy gaps of 1.91 and 0.99 eV between the emissive states ^{3}ILCT/$^3LMCT_{py}$ and the ^{1}GS (Fig. 8a, 9a and Table 3) and the different SOC contribution promoting ISC to the ^{1}GS in the ^{3}ILCT (smaller SOC) and ^{3}LMCT (higher SOC) states, respectively, together with the smaller heavy-atom effect for Sn, compared to Pb.

The excited state dynamics of $\mathbf{1}^{\mathbf{Sn}}$ in frozen 2-Me-THF might additionally be affected by solvent coordination during freezing and hence the presence of different solvates in the frozen sample, *e.g.* $\mathbf{1}^{\mathbf{Sn}}$**(2-Me-thf)**$_n$, which might account for the multiple emission lifetimes. Consequently, TD-DFT calculations were performed on $\mathbf{1}^{\mathbf{Sn}}$**(thf)**. Similar to $\mathbf{1}^{\mathbf{Sn}}$, the lowest Franck–Condon states are of ^{1}ILCT character, slightly shifted to higher energies (ESI, Fig. S29–31†).

The Sn–O^{thf} distance of 2.606 Å in the ^{1}GS increases to 2.925 Å in the ^{3}ILCT state, while the Sn–N distances are essentially unchanged, according to DFT calculations (Fig. 3b and 11a; ESI, Table S1†). This suggests that the initially populated ^{3}ILCT state of the adduct $\mathbf{1}^{\mathbf{Sn}}$**(thf)** is strongly distorted. The deactivation of the ^{3}ILCT state occurs preferentially *via* the $^3LMCT_{py}$ state suggested by a 2D relaxed triplet surface scan as a projection along the Sn–O^{thf} and Sn–N^{py} modes (Fig. 12). The trajectory for ^{3}ILCT/$^3LMCT_{py}$ internal conversion follows the Sn–O^{thf} coordinate with THF dissociation, forming donor-free $\mathbf{1}^{\mathbf{Sn}}$ within the ^{3}ILCT state and then converts to the $^3LMCT_{py}$ state along the Sn–N^{py} coordinate (Fig. 12). The $^3LMCT_{py}$ state is slightly destabilised relative to the ^{3}ILCT in the loose van-der-Waals adduct between THF and $\mathbf{1}^{\mathbf{Sn}}$ in $\mathbf{1}^{\mathbf{Sn}}$**(thf)** (Tables 3 and 4; ESI, Tables S3 and S4†). A relaxed surface scan on the ^{3}ILCT surface along the Sn–O^{thf} stretching mode shows that THF dissociation is essentially barrierless (Fig. 11a). Additionally, a ^{3}MLCT and a $^3LMCT_{pyr}$ state with dissociated pyrrolato moiety and THF, could be located as local minima for the THF adduct $\mathbf{1}^{\mathbf{Sn}}$**(thf)** at higher energies (Fig. 11; ESI, Table S1†). The geometries of the relaxed ^{3}MLCT and ^{3}ILCT states mainly differ by their Sn–O^{thf} distances and N^{py}–Sn–O^{thf} angles δ_3, in accordance to the valence shell electron pair repulsion model as simplest explanation (Fig. 11a; ESI, Table S1†). Due to their comparably high energy, these ^{3}MLCT and $^3LMCT_{pyr}$ states should not play a significant role in the deactivation of the phosphorescent ^{3}ILCT state (Table 4; ESI, Table S4†).

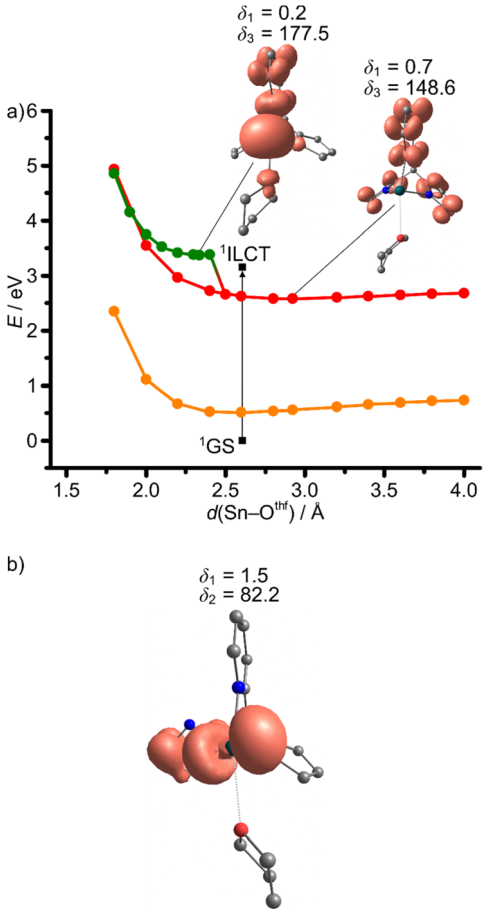

Fig. 11 (a) Relaxed potential energy surface scans as projections along the Sn–O^{thf} stretching mode on the triplet hypersurface $^3\mathbf{1}^{\mathbf{Sn}}$**(thf)** with selected geometry optimised molecular structures with spin densities and single point energies on singlet GS hypersurface $^1\mathbf{1}^{\mathbf{Sn}}$**(thf)** at $^3\mathbf{1}^{\mathbf{Sn}}$**(thf)** geometries (SCF energies). ^{3}ILCT state indicated in red, ^{3}MLCT state in green and ^{1}GS in orange. Vertical transition from relaxed ^{1}GS to the ^{1}ILCT state from TD-DFT calculations (3.15 eV) indicated as black arrow. (b) Molecular structure of the $^3LMCT_{pyr}$ state with spin density. Spin density isosurface values are at 0.005 a.u. Selected Sn–$N^{py/pyr}$–$C^{py/pyr}$–$C^{backbone}$ dihedral angles δ_1/δ_2 and N^{py}–Sn–O^{thf} angles δ_3 in deg. are indicated. CPCM-(THF)-RIJCOSX-(U)B3LYP-D3BJ-ZORA/def2-TZVPP/old-ZORA-TZVPP(Sn).

In summary, the calculations suggest that donor-free $\mathbf{1}^{\mathbf{Sn}}$ shows emission from a weakly distorted ^{3}ILCT state (non-Kasha behavior) due to high enough barriers to the ^{3}LMCT states, while $\mathbf{1}^{\mathbf{Pb}}$ efficiently evolves from the initially populated nested ^{3}ILCT state to the dissociative, low-energy, weakly emissive $^3LMCT_{py}$ state. Compared to the often weakly distorted CT states of photoluminescent TMCs,[1–3] the low-energy ^{3}LMCT states observed here are highly distorted. Clearly, this arises from the rather non-bonding character of the involved transition metal d-orbitals, while ^{3}LMCT states of $\mathbf{1}^{\mathbf{Sn}}$ and $\mathbf{1}^{\mathbf{Pb}}$ are characterised by the population of σ*(E–X) orbitals leading to large distortions and even donor moiety dissociation (pyridine or pyrrolato). Excited states of ^{3}MLCT nature involving the non-bonding tetrel-centered lone-pair of high s character would be

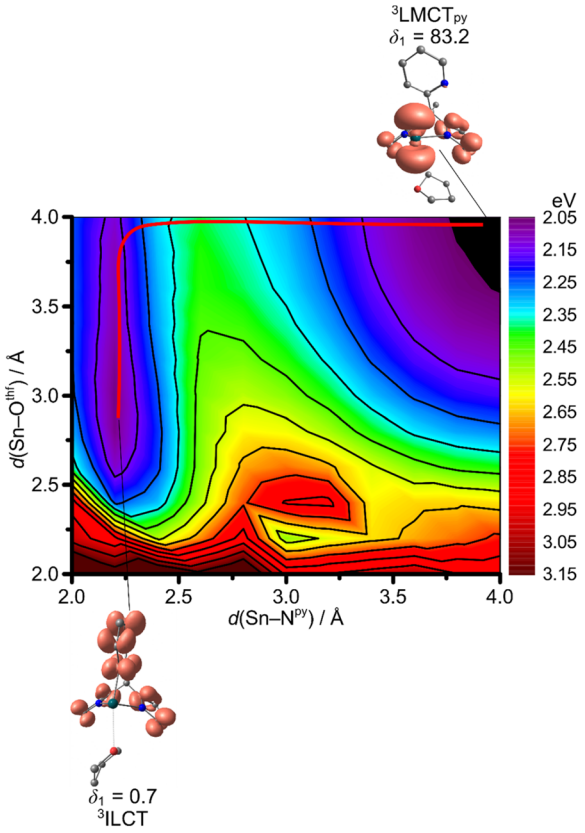

Fig. 12 Contour plot of a 2D relaxed potential energy surface scan as projection along the Sn–N^{py} and Sn–O^{thf} stretching modes on the triplet hypersurface ^{3}**1**^{Sn}**(thf)** with selected geometry optimised molecular structures with spin densities (isosurface value: 0.005 a.u.). Selected E–N^{py}–C^{py}–C^{backbone} dihedral angles δ_1 in deg. are indicated and the graphically determined, estimated minimum energy path for ^{3}ILCT → ^{3}LMCT$_{py}$ (red line) internal conversion. Energies are given *vs.* the ^{1}GS energy (ESI, Fig. S32†). CPCM-(THF)-RIJCOSX-UB3LYP-D3BJ-ZORA/def2-TZVPP/old-ZORA-TZVPP(Sn).

Table 4 Relative energies (SCF)[a] of triplet states and ^{1}GS in eV, calculated by DFT for **1**^{Sn}**(thf)**

^{3}ILCT	0
^{3}LMCT$_{py}$	−0.11
^{3}MLCT	+0.79
^{3}LMCT$_{pyr}$	+0.10
^{1}GS$_{relaxed}$[b]	−2.58
^{1}GS$_{^3ILCT\text{-}geom}$[c]	−2.02
^{1}GS$_{^3LMCT_{py}\text{-}geom}$[c]	−1.15
^{1}GS$_{^3MLCT\text{-}geom}$[c]	−1.55
^{1}GS$_{^3LMCT_{pyr}\text{-}geom}$[c]	−0.73

[a] For Gibbs free energies, see: ESI, Table S4. [b] Relaxed geometry. [c] ^{1}GS at relaxed ^{3}ILCT, ^{3}LMCT$_{py}$, ^{3}MLCT and ^{3}LMCT$_{pyr}$ geometry, respectively.

less distorted. Such ^{3}MLCT states indeed exist, yet at higher energies than the dissociative ^{3}LMCT states in **1**^{Sn} and **1**^{Pb} (Fig. 1 and 4; ESI, Fig. S17 and S18†). ^{3}LMCT states involving the empty p-type orbital in non-donor stabilised tetrylenes might provide another weakly distorted and potentially emissive CT state in tetrylenes.

3 Conclusions

Sn^{II}(bpep) **1**^{Sn} shows phosphorescence from an ^{3}ILCT state (non-Kasha behavior) in solution and in the solid state. The phosphorescence quantum yield and the photoluminescence lifetime drastically increase from $\tau_{p,293} = 14$ ns, $\Phi_{p,293} = 0.005$ to $\tau_{p,77} = 3.6$ ms, $\Phi_{p,77} = 0.58$ from 293 to 77 K in the solid state. In contrast, Pb^{II}(bpep) **1**^{Pb} shows very weak short-lived phosphorescence at 77 K ($\tau_{p,77} = 92$ ns, $\Phi_{p,77} = 0.0024$) with strong decrease in lifetime to $\tau_{p,200} = 2.4$ ns at 200 K. This photoluminescence arises from a ^{3}LMCT state, populated *via* IC from the initially populated ^{3}ILCT state. The strong temperature dependence is attributed to two thermally activated processes with experimentally determined barriers of $E_{a_1} = 0.25$ eV and $E_{a_2} = 0.10$ eV for **1**^{Sn} and $E_{a_1} = 0.11$ eV and $E_{a_2} = 0.02$ eV for **1**^{Pb}. Two strongly distorted, dissociative ^{3}LMCT states, according to (2D) relaxed potential energy surface scans by DFT calculations, open up pathways for fast (non-radiative) deactivation of the nested ^{3}ILCT state. The corresponding barrier is significantly lower for **1**^{Pb} (0.06/0.06 eV) than for **1**^{Sn} (0.23/0.25 eV, DFT SCF/Gibbs free energies). ISC is fast despite the weak contribution of the Sn and Pb atoms to the excited state wavefunctions of the initially populated ^{1}ILCT state. The expectedly larger heavy-atom effect, leading to faster ISC of the lead compound **1**^{Pb}, is compensated by the much faster deactivation due to the significantly smaller barriers, obtained from variable-temperature photoluminescence lifetime measurements and supported by DFT calculations. In solution, the population of the ^{3}ILCT state of the THF adduct **1**^{Sn}**(thf)** is accompanied with solvent decoordination and formation of **1**^{Sn}.

In order to obtain phosphorescent tetrel(II) complexes, the focus should not be kept solely on the heavy-atom effect, invoking effective SOC to enable fast singlet-to-triplet ISC, but also on the ES ordering, enabling fast non-radiative deactivation of potential phosphorescent ESs. Geometric excited state reorganisation and solvent (de-)coordination seems to play a more pronounced role for tetrylenes than for pseudo-octahedral TMCs, but seems comparable to pseudo-tetrahedral Cu^{I} complexes with their ES flattening distortion, prone to solvent or anion coordination.

With the energy landscape of **1**^{E} (E = Sn, Pb), obtained from this initial study, a rational optimisation of the photoluminescent properties emerges. (1) The ^{3}ILCT state should be pushed to energies below the ^{3}LMCT states with electron-withdrawing substituents on the pyridine moieties. (2) The ^{3}LMCT states could be pushed to higher energies with the lighter homologues germanium and silicon, probably with higher ^{3}ILCT/^{3}LMCT barriers by decreased molecular flexibility. (3) Rigidification of the pyridine moiety with bulky substituents could prevent the dissociation and torsional motion of the pyridine. (4) Lowering the energy of the tentatively weakly distorted ^{3}MLCT states below the ^{3}ILCT and ^{3}LMCT states to obtain ^{3}MLCT phosphorescence. (5) Mitigating the dissociative character of the ^{3}LMCT states in non-donor stabilised tetrylenes. Current investigations in these directions are in progress.

Data availability

All experimental and computational data are available in the ESI.† Crystallographic data have been deposited in the Cambridge Crystallographic Data Centre under accession numbers CCDC 2211125 and 2211126.

Author contributions

P. S. performed the synthesis and characterisation as well as (TD-)DFT calculations. R. N. and P. S. measured and interpreted the emission data. C. F. solved the single crystal structures. C. F. conceived and designed the project. C. F. wrote the manuscript with contributions of all authors. K. H. supervised and C. F. co-supervised the project.

Conflicts of interest

There are no conflicts to declare.

Acknowledgements

This work has been financially supported by the Deutsche Forschungsgemeinschaft (DFG) under grant INST 247/1018-1 (K. H.). Parts of this research were conducted using the supercomputer Elwetritsch and advisory services offered by the University of Kaiserslautern-Landau (**https://hpc.rz.rptu.de**), which is a member of the AHRP and the Gauss Alliance e.V. We thank Dr Dieter Schollmeyer for collecting the XRD data and Dr Mihail Mondeshki for ^{119}Sn and ^{207}Pb NMR measurements.

References

1 C. Wegeberg and O. S. Wenger, *JACS Au*, 2021, **1**, 1860–1876.
2 C. Förster and K. Heinze, *Chem. Soc. Rev.*, 2020, **49**, 1057–1070.
3 O. S. Wenger, *Chem.–Eur. J.*, 2019, **25**, 6043–6052.
4 B. M. Hockin, C. Li, N. Robertson and E. Zysman-Colman, *Catal. Sci. Technol.*, 2019, **9**, 889–915.
5 C. B. Larsen and O. S. Wenger, *Chem.–Eur. J.*, 2018, **24**, 2039–2058.
6 V. Balzani, P. Ceroni and A. Juris, *Photochemistry and Photophysics. Concepts, Research, Applications*, Wiley-VCH, Weinheim, 1st edn, 2014.
7 T. J. Penfold, E. Gindensperger, C. Daniel and C. M. Marian, *Chem. Rev.*, 2018, **118**, 6975–7025.
8 M. Iwamura, S. Takeuchi and T. Tahara, *Acc. Chem. Res.*, 2015, **48**, 782–791.
9 N. Armaroli, *Chem. Soc. Rev.*, 2001, **30**, 113–124.
10 C. Sandoval-Pauker, M. Santander-Nelli and P. Dreyse, *RSC Adv.*, 2022, **12**, 10653–10674.
11 Y. Zhang, M. Schulz, M. Wächtler, M. Karnahl and B. Dietzek, *Coord. Chem. Rev.*, 2018, **356**, 127–146.
12 S. A. Patra, G. Sahu, P. D. Pattanayak, T. Sasamori and R. Dinda, *Inorg. Chem.*, 2022, **61**, 16914–16928.
13 J. C. Berrones-Reyes, C. C. Vidyasagar, B. M. Muñoz Flores and V. M. Jiménez-Pérez, *J. Lumin.*, 2018, **195**, 290–313.
14 D. S. M. Ravinson and M. E. Thompson, *Mater. Horiz.*, 2020, **7**, 1210–1217.
15 H. Yersin, R. Czerwieniec, M. Z. Shafikov and A. F. Suleymanova, *ChemPhysChem*, 2017, **18**, 3508–3535.
16 H. Yersin, A. F. Rausch, R. Czerwieniec, T. Hofbeck and T. Fischer, *Coord. Chem. Rev.*, 2011, **255**, 2622–2652.
17 S. Arunkumar, D. Ghosh and G. R. Kumar, *Results Chem.*, 2022, **4**, 100399.
18 S. M. Parke and E. Rivard, *Isr. J. Chem.*, 2018, **58**, 915–926.
19 S. M. Parke, M. P. Boone and E. Rivard, *Chem. Commun.*, 2016, **52**, 9485–9505.
20 L. A. Maurer, O. M. Pearce, F. D. R. Maharaj, N. L. Brown, C. K. Amador, N. H. Damrauer and M. P. Marshak, *Inorg. Chem.*, 2021, **60**, 10137–10146.
21 A. K. Adcock, R. L. Ayscue, L. M. Breuer, C. P. Verwiel, A. C. Marwitz, J. A. Bertke, V. Vallet, F. Réal and K. E. Knope, *Dalton Trans.*, 2020, **49**, 11756–11771.
22 S. M. Parke, E. Hupf, G. K. Matharu, I. de Aguiar, L. Xu, H. Yu, M. P. Boone, G. L. C. de Souza, R. McDonald, M. J. Ferguson, G. He, A. Brown and E. Rivard, *Angew. Chem., Int. Ed. Engl.*, 2018, **57**, 14841–14846.
23 S. M. Parke, M. A. B. Narreto, E. Hupf, R. McDonald, M. J. Ferguson, F. A. Hegmann and E. Rivard, *Inorg. Chem.*, 2018, **57**, 7536–7549.
24 O. Toma, M. Allain, F. Meinardi, A. Forni, C. Botta and N. Mercier, *Angew. Chem., Int. Ed.*, 2016, **55**, 7998–8002.
25 O. Toma, N. Mercier, M. Allain, A. Forni, F. Meinardi and C. Botta, *Dalton Trans.*, 2015, **44**, 14589–14593.
26 O. Toma, N. Mercier and C. Botta, *Eur. J. Inorg. Chem.*, 2013, 1113–1117.
27 A. Strasser and A. Vogler, *Inorg. Chem. Commun.*, 2004, **7**, 528–530.
28 Y. Kang, D. Song, H. Schmider and S. Wang, *Organometallics*, 2002, **21**, 2413–2421.
29 D. Temerova, T.-C. Chou, K. S. Kisel, T. Eskelinen, N. Kinnunen, J. Jänis, A. J. Karttunen, P.-T. Chou and I. O. Koshevoy, *Inorg. Chem.*, 2022, **61**, 19220–19231.
30 A. S. Gowda, T. S. Lee, M. C. Rosko, J. L. Petersen, F. N. Castellano and C. Milsmann, *Inorg. Chem.*, 2022, **61**, 7338–7348.
31 M. Kocherga, J. Castaneda, M. G. Walter, Y. Zhang, N.-A. Saleh, L. Wang, D. S. Jones, J. Merkert, B. Donovan-Merkert, Y. Li, T. Hofmann and T. A. Schmedake, *Chem. Commun.*, 2018, **54**, 14073–14076.
32 D. Maeda, H. Shimakoshi, M. Abe and Y. Hisaeda, *Inorg. Chem.*, 2009, **48**, 9853–9860.
33 A. Endo, M. Ogasawara, A. Takahashi, D. Yokoyama, Y. Kato and C. Adachi, *Adv. Mater.*, 2009, **21**, 4802–4806.
34 W.-L. Jia, Q.-D. Liu, R. Wang and S. Wang, *Organometallics*, 2003, **22**, 4070–4078.
35 M. Gouterman, F. P. Schwarz, P. D. Smith and D. Dolphin, *J. Chem. Phys.*, 1973, **59**, 676–690.
36 M. Kocherga, K. M. Boyle, J. Merkert, T. A. Schmedake and M. G. Walter, *Mater. Adv.*, 2022, **3**, 2373–2379.

37 J. Hoffmann, I.-M. Ramirez Y Medina, M. Hissler and A. Staubitz, *Dalton Trans.*, 2021, **50**, 6213–6221.
38 M. Gon, K. Tanaka and Y. Chujo, *Chem.–Eur. J.*, 2021, **27**, 7561–7571.
39 I.-M. Ramirez Y Medina, M. Rohdenburg, W. Kipke, E. Lork and A. Staubitz, *Molecules*, 2020, **25**, 4993.
40 I.-M. Ramirez Y Medina, M. Rohdenburg, E. Lork and A. Staubitz, *Chem. Commun.*, 2020, **56**, 9775–9778.
41 W. Ki, K. Ngo, P. Ghosh, B. Averkiev, G. T. Reeves, I. Ailes, B. C. Pemberton, K. Zhu and J. Li, *Chem. Commun.*, 2020, **56**, 9648–9650.
42 M. Yamamura, M. Albrecht, M. Albrecht, Y. Nishimura, T. Arai and T. Nabeshima, *Inorg. Chem.*, 2014, **53**, 1355–1360.
43 K. Takano, M. Takahashi, T. Fukushima, M. Takezaki, T. Tominaga, H. Akashi, H. Takagi and T. Shibahara, *Bull. Chem. Soc. Jpn.*, 2012, **85**, 1210–1221.
44 S. M. Crawford, A. Al-Sheikh Ali, T. S. Cameron and A. Thompson, *Inorg. Chem.*, 2011, **50**, 8207–8213.
45 R. Ballardini, G. Varani, M. T. Indelli and F. Scandola, *Inorg. Chem.*, 1986, **25**, 3858–3865.
46 H. Nikol, A. Becht and A. Vogler, *Inorg. Chem.*, 1992, **31**, 3277–3279.
47 K. Oldenburg and A. Vogler, *Z. Naturforsch., B: J. Chem. Sci.*, 1993, **48**, 1519–1523.
48 A. Becht and A. Vogler, *Z. Naturforsch., B: J. Chem. Sci.*, 1994, **49**, 778–780.
49 A. Strasser and A. Vogler, *J. Photochem. Photobiol., A*, 2004, **165**, 115–118.
50 L.-X. Wang, J. Xiang, D. Xiang, S.-C. Cheng, C.-F. Leung and C.-C. Ko, *Inorg. Chem.*, 2022, **61**, 16831–16840.
51 J. Kobayashi, T. Kushida and T. Kawashima, *J. Am. Chem. Soc.*, 2009, **131**, 10836–10837.
52 J.-D. Guo, D. J. Liptrot, S. Nagase and P. P. Power, *Chem. Sci.*, 2015, **6**, 6235–6244.
53 Y. Mizuhata, T. Sasamori and N. Tokitoh, *Chem. Rev.*, 2009, **109**, 3479–3511.
54 K. W. Klinkhammer, in *The Chemistry of Organic Germanium, Tin and Lead Compounds*, ed. Z. Rappoport, John Wiley Sons Ltd, Chichester, 2nd edn, 2002, vol. 2, pp. 283–357.
55 N. Tokitoh and R. Okazaki, *Coord. Chem. Rev.*, 2000, **210**, 251–277.
56 P. P. Power, *Chem. Rev.*, 1999, **99**, 3463–3504.
57 G. Gao, I. Korobkov and S. Gambarotta, *Inorg. Chem.*, 2004, **43**, 1108–1115.
58 M. Montalti and S. L. Murov, *Handbook of Photochemistry*, CRC/Taylor & Francis, Boca Raton, 3rd edn, 2006.
59 M. J. S. Gynane, D. H. Harris, M. F. Lappert, P. P. Power, P. Rivière and M. Rivière-Baudet, *Dalton Trans.*, 1977, 2004–2009.
60 J. D. Parish, M. W. Snook, A. L. Johnson and G. Kociok-Köhn, *Dalton Trans.*, 2018, **47**, 7721–7729.
61 M. Kira, S. Ishida, T. Iwamoto, R. Yauchibara and H. Sakurai, *J. Organomet. Chem.*, 2001, **636**, 144–147.
62 A. J. Lees, *Comments Inorg. Chem.*, 1995, **17**, 319–346.
63 F. Barigelletti, D. Sandrini, M. Maestri, V. Balzani, A. von Zelewsky, L. Chassot, P. Jolliet and U. Maeder, *Inorg. Chem.*, 1988, **27**, 3644–3647.
64 A. Gonzalez, E. S. Kengmana, M. V. Fonseca and G. Han, *Mater. Today Adv.*, 2020, **6**, 100058.
65 C. L. Linfoot, M. J. Leitl, P. Richardson, A. F. Rausch, O. Chepelin, F. J. White, H. Yersin and N. Robertson, *Inorg. Chem.*, 2014, **53**, 10854–10861.
66 S. Suzuki, S. Sasaki, A. S. Sairi, R. Iwai, B. Z. Tang and G.-I. Konishi, *Angew. Chem., Int. Ed.*, 2020, **59**, 9856–9867.
67 R. Crespo-Otero, Q. Li and L. Blancafort, *Chem.–Asian J.*, 2019, **14**, 700–714.
68 L. Ravotto and P. Ceroni, *Coord. Chem. Rev.*, 2017, **346**, 62–76.